Transactions of the Canadian Society for Mechanical Engineering, Available online 24 March 2022
DOI:10.1139/tcsme-2021-0205

Numerical Investigation of Fluid Flow and Heat Characteristics of a Roughened Solar Air Heater with Novel V-shaped Ribs

Usman Allauddin[1*], Waqar A. Khan[2], Saim E. Ali [1], Syed M.M. Haider[1], Abdul S. Ahmed[1], Abdur Rehman[1], Patrick G. Verdin[3]

[1] *Department of Mechanical Engineering, NED University of Engineering & Technology, Karachi 75270, Pakistan*

[2] *Prince Mohammad Bin Fahd University, Department of Mechanical Engineering, Al Khobar 31952, Kingdom of Saudi Arabia*

[3] *Energy & Power, School of Water, Energy & Environment, Cranfield University, Cranfield MK43 0AL, United Kingdom*

[*] Corresponding author
E-mail: usman.allauddin@neduet.edu.pk
Mailing Address: Department of Mechanical Engineering, NED University of Engineering & Technology, Karachi 75270, Pakistan

ABSTRACT

Solar air heaters convert clean solar energy into useful heat and have a wide range of applications. Computational Fluid Dynamics (CFD) can aid in the design and development of solar air heaters with optimized thermal efficiency. A detailed numerical study was conducted to investigate the fluid flow and heat transfer characteristics of a roughened solar air heater with novel V-shaped ribs having staggered elements. Three dimensional steady-state numerical simulations were performed using the $k-\varepsilon$ RNG turbulence model, and results were found in excellent agreement with experimental data. The effect of ribs spacing were studied through varying the rib pitch to rib height ratio $P/e = 6$ to 14, for Reynolds numbers (Re) in the range of 4000-14,000. A significant enhancement in the ribs-roughened solar air heater's thermal performance was observed. It was also established that an increment in P/e from 6 to 10 increases the Nusselt number (Nu) for all Re values investigated. About 72.6% Nu enhancement was predicted for $P/e = 10$ at Re = 12,000. It was further observed that an increment in p/e from 10 to 14 decreases Nu for all Re values considered.

Keywords:

Solar air heater, heat transfer enhancement, surface enlargement elements, ribs, Nusselt number.

NOMENCLATURE

C_p	Specific heat capacity [J kg^{-1} K^{-1}]
D_h	Hydraulic diameter [m]
h	Convection heat transfer coefficient [W m^{-2} K^{-1}]
k	Turbulence kinetic energy [m^2 s^{-2}]
Nu	Nusselt Number [-]
p	Pressure [Pa]
q	Heat flux [W m^{-2}]
Re	Reynolds Number [-]
T	Temperature [K]
T_i	Air temperature at channel inlet [K]
T_o	Air temperature at channel outlet [K]
T_m	Mean air temperature [K]
U	Velocity [m s^{-1}]
y^+	Dimensionless wall normal distance [-]

Greek symbols:

ε	Turbulence dissipation [m^2 s^{-3}]
λ	Thermal conductivity [W m-1 K-1]
μ	Dynamic viscosity [Pa s]
v	Kinematic viscosity [m^2 s^{-1}]
ρ	Density [kg m^{-3}]

Geometric Parameters:

e	Rib height [m]
g	Gap width of symmetric rib elements [m]
g'	Width of the relative gap in each symmetrical rib elements [m]
H	Height of channel [m]
L	Length of channel [m]
P	Rib pitch [m]
P'	Position of staggered element [m]
r	Size of the staggered rib element [m]
w	Vertical length of symmetrical rib elements [m]
W	Width of channel [m]
α	Angle of attack [Radian]

Subscript:

avg	Averaged

1. INTRODUCTION

The current energy scenario has created a need for more efficient and environmentally less harmful heat exchange devices compared to the existing ones. Solar Air Heaters (SAHs) completely fulfills the aforementioned criteria. SAHs have a wide range of applications in the

industrial, residential and agricultural sectors (Close 1963; Selcuk 1977). The usage of SAHs is expected to be significantly increased in the near future because of their attractive features such as low weight, simple design, ease of fabrication at low cost and their use of green solar energy. The only problem is that conventional SAHs have a very low thermal efficiency. An extensive research has been carried out to improve SAHs' thermal efficiency. One of the available methods is the passive method, where the absorber plate surface area and turbulence of the air flow over the target plate are increased by using different surface enlargement elements. Over the last few years, different novel designs of solar air heaters with a unique shape and combination of surface enlargement elements have been experimentally investigated (Arunkumar et al. 2020; Bisht et al. 2018; Chhaparwal et al. 2019; Jain et al. 2019; Singh and Singh 2018; Alam and Kim 2017; Ravi and Saini 2016; Kumar et al. 2020; Saxena et al. 2015). Extensive literature reviews focusing on the different techniques to enhance SAHs' thermal performance are available through review articles (Kumar et al. 2020; Saxena et al. 2015). Several researchers have also discussed the state of the art studies in the area of the SAHs thermal performance improvement using surface enlargement elements (Arunkumar et al. 2020; Bisht et al. 2018; Chhaparwal et al. 2019; Jain et al. 2019; Singh and Singh 2018; Alam and Kim 2017; Ravi and Saini 2016). Recently, Arunkumar et al. (2020) reported a comprehensive review of the studies focusing on the thermal performance enhancement of SAHs with different design modifications e.g. collector shape, flow passage and absorber plate modifications. The authors summarized a variety of seventy three studies and reported effects of different design modifications on the temperature of the absorber plate, the air temperature at the heater outlet, the Nusselt number (Nu) of the absorber plate and overall thermo-hydraulic performance parameter of SAHs. The authors concluded that the roughened SAHs offer better thermal performance at low to moderate Reynolds numbers (Re). The authors also urged a more extensive utilization of numerical simulation for the modelling of short- and long-term

performance of roughened SAHs to obtain an optimized design, especially at high Re. Bisht et al. (2018) reviewed a variety of experimental studies dealing with the roughened solar heaters reported in the open literature. With intent to find out the best turbulator, the authors compared the thermal performance of SAHs with commonly used turbulators. The Nusselt number Nu, thermo-hydraulic performance parameters and thermal efficiency of SAHs roughened with different shapes and arrangement pattern of turbulators were comprehensively compared. The authors, in general, concluded that a significant improvement in the thermal performance of SAHs could be obtained with any type of artificial roughness, but the maximum thermal performance was observed with arrays of V-shaped ribs when arranged with suitable gaps. Looking at the significant thermal performance enhancement with V-shaped ribs, the authors also proposed a possible area of research investigating the SAH performance roughened with circular protrusions arranged in a V-shaped pattern. Jain et al. (2019) reported a concise review of 124 different studies related to thermal performance investigation of solar air heaters roughened with a V-shaped pattern. The authors reported a superior performance of SAHs roughened with a V-shaped pattern as compared to the other available patterns. The V-shaped pattern is thus a preferable choice because of the ease of fabrication. Secondly, the ribs arranged in V-shaped pattern produce a better mixing of secondary and primary flows, making the laminar viscous sublayer turbulent. The flow separation and reattachment are also relatively better. The authors predicted a future trend of more extensive use of Computational Fluid Dynamics (CFD) based numerical studies for an advanced level study of roughened solar air heaters. Chhaparwal et al. (2019) reviewed a variety of SAHs' thermal performance investigation studies, encompassing fifty different varieties of turbulators. The authors concluded that the performance of roughened SAHs is mostly investigated through experimental and analytical studies. Only a few numerical studies are reported, defining a suitable numerical model for an accurate prediction of heat transfer and fluid flow

characteristics of roughened SAHs. The authors encouraged the research community working on SAHs, to perform comprehensive CFD-based numerical studies that can complement experimental and analytical studies, to design an optimized roughened solar heater.

A variety of combinations of V-shaped ribs are experimentally investigated in solar air heaters. A few examples are single V-continuous (Lau et al. 1991), multiple V-continuous (Promvonge 2010), single V-broken/discrete (Tanda 2004), multiple V-broken/discrete (Kumar et al. 2014), single V-staggered (Patil 2012), multiple V-staggered (Kumar and Kim 2015), single V-perforation/holes (Alam et al. 2014), multiple V-perforation/holes (Kumar et al. 2017a), single V-shaped dimple ribs (Kumar et al. 2017b), multiple V-shaped dimple ribs (Kumar et al. 2017c), V-ribs with wavy arrangement (Khanoknaiyakarn et al. 2011), combined V-shapped (Boonloi and Jedsadaratanachai 2016), etc. Bisht et al. (2018) compared the performance of several shapes and orientations of the ribs in SAH cases. They reported that the V-shaped ribs having gaps would produce the highest values of Nu at all Re. Patel and Lanjewar (2018) studied the convective heat transfer coefficient's amplification in a repeated V-pattern with tottered ribs. They reported that the roughness induced an amplification of 4.28 times Nu as compared to the smooth absorber plate. Chamoli and Thakur (2013) reported a 78% increase in effective efficiency by using V-down baffles with perforation in SAHs. Maithani and Saini (2016) studied the convective coefficient with artificially roughened duct using V-ribs with symmetrical gaps as a turbulence promoter. Patel and Lanjewar (2019) artificially roughened the absorber plate by using the novel multiple V-discrete ribs geometry to increase the convective heat transfer coefficient. They concluded that for all p/e values, Nu increases with increasing Re. Jin et al. (2015) reported that repeating V-shaped ribs generates stream-wise helical vortex flows, encouraging the fluid homogeneity between the cold and the warm fluid. It was observed that Nu, Friction factor, and Thermo-hydraulic performance parameters reduced with the rise in relative pitch. Yadav and Thapak (2014) experimentally investigated

a roughened SAH with different kinds of rough geometries. They reported that the highest Nu and friction factors were achieved using a multi-V-rib with gaps. Karwa and Srivastava (2013) observed SAH's performance with the roughness of a V- down Discrete Rib. It was reported that the efficiency of SAHs was increased by 6 and up to 26% compared to the smooth duct air heater.

CFD-based modelling techniques have improved drastically with the recent advances in computational facilities. They can now be efficiently used to identify the optimum geometrical configuration of a roughened SAH before going through experimental testing, which is expensive and time consuming. Several researchers have numerically investigated a variety of roughened solar heaters. Gawande et al. (2016) reviewed different numerical and analytical studies, focusing on the design of a solar heater offering an optimum thermo-hydraulic performance. Around fifty numerical studies were reviewed and CFD-based techniques were reported to be efficient in generating numerical results in agreement with previously obtained experimental data. CFD-based studies encompass a wide class of roughened solar heaters. Several researchers have investigated the performance of SAHs roughened with circular-sectioned transverse ribs, chamfered ribs, right angle triangular ribs, semi-circular transverse ribs, inclined ribs with gaps, equilateral triangular sectioned ribs, inclined circular ribs, square-sectioned transverse ribs, triangular-sectioned transverse ribs, square ribs, triangular ribs, circular transverse wire ribs, square type protrusion, U-type turbulators, K-shaped ribs, V-shaped ribs, L-shaped ribs, etc., (Gawande et al. 2016).

The literature review shows that only few CFD-based numerical studies for roughened SAHs, especially roughened with V-shaped ribs, were reported, compared to available experimental studies. Numerical studies can aid in the design and development of novel SAHs, offering an optimum thermo-hydraulic performance. In the current work, the fluid flow and heat transfer

characteristics of a roughened SAH with novel V-shaped ribs having staggered arrangement are investigated and discussed.

2. GOVERNING EQUATIONS

CFD is applied for the numerical work. The governing equations in the differential form are given by:

$$\frac{\partial U_i}{\partial x_i} \tag{1}$$

$$\frac{\partial\left(\rho U_j U_i\right)}{\partial x_j} = -\frac{\partial p}{\partial x_i} + \frac{\partial}{\partial x_j}\left[\mu\left(\frac{\partial U_i}{\partial x_j} + \frac{\partial U_j}{\partial x_i}\right) - \rho\overline{U_i' U_j'}\right] \tag{2}$$

$$\frac{\partial(\rho U_i T)}{\partial x_i} = \frac{\partial}{\partial x_i}\left[k\frac{\partial T}{\partial x_i} - \rho C_p\overline{U_i' T'}\right] \tag{3}$$

where P, T, U_i, ρ, and μ stand for the mean pressure, temperature, velocity component, fluid density, and dynamic viscosity, respectively while T' and U_i' denote the fluctuating temperature and velocity components in the x_i direction.

For Reynolds Average Navier-Stokes (RANS) modelling, the choice of turbulence model plays a critical role for an accurate modelling of the actual flow and thermal physics of SAH systems. Many researchers have extensively investigated the performance of available turbulence models in predicting the correct behaviors of SAH systems (Yadav and Bhagoria 2013a; Yadav and Bhagoria 2013b). These sensitivity studies show the RNG $k-\varepsilon$ model as the most effective turbulence model, offering an accurate thermal performance of SAH systems. Kumar and Saini (2009); Karmare and Tikeker (2010); Yadav et al. (2013); Yadav and Bhagoria (2013c) also reported the good performance of the RNG $k-\varepsilon$ turbulence model in predicting the thermal performance of solar air heaters. In the current work, the RNG $k-\varepsilon$ turbulence model is therefore selected. Readers are referred to (ANSYS Fluent 2016) for a detailed explanation and complete set of equations for this model.

3. COMPUTATIONAL MODEL

Figure 1a shows the computational domain used in the current study. The geometry was created within the ANSYS Workbench software using the Design Modeler utility. The computational domain was divided into three sections: inlet section, test section and outlet section. The inlet, test and outlet sections of the channel were 800 mm, 1000 mm and 550 mm long, respectively. The inlet and outlet sections were created long enough to provide stability in the system, ensure that the flow has developed when reaching the test section, and prevent divergence problems from happening during the numerical simulations.

The width (W) and height (H) of the channel are 300 mm and 25mm, respectively. Figure 1b shows the schematic illustration of the ribs arrangement on the absorber plate. These ribs are arranged in a V-shaped, repeated, discrete and staggered pattern. Figure 1c illustrates different geometrical parameters of the V-shaped ribs. The values of different geometrical parameters of the computational domain and V-shaped ribs are tabulated in Table 1. Five different simulation cases (I, II, III, IV and V) were developed by changing the rib pitch to rib height ratio P/e from 6 to 14. The geometrical parameters of these five cases are listed in Table 2. Figure 2a shows the boundary conditions used during the numerical simulations. A velocity-inlet boundary condition with a temperature of 300 K and a turbulence intensity of 5% is used at the inlet. A pressure outlet boundary condition is applied at the outlet, allowing backflow in the flow domain at atmospheric pressure. The target plate was modeled with a constant heat flux wall boundary condition, with a heat flux value of 1000 W/m^2. The remaining surfaces were modeled using a no-slip adiabatic wall boundary condition.

Figure 2b shows the schematic illustration of one of the meshes used in the numerical simulations. All the meshes were unstructured, having triangular prism elements; they were generated with the meshing utility within ANSYS Workbench. Inflation layers were created to

fully capture the boundary layer near the walls. The first layer thickness was set according to the appropriate y+ values required for the turbulence model. The enhanced wall treatment is used for near wall flow modelling with y+ < 1.

Three-dimensional numerical simulations of air as the working fluid, were performed with ANSYS FLUENT 16.0., using the steady-state solver, and ignoring gravity (body forces). The Semi-Implicit Method for Pressure-Linked Equations (SIMPLE) algorithm with the 1st order upwind discretization scheme for all governing equations was applied, and a convergence criterion of 10^{-6} was set for all equations. Note that a 1st order discretization scheme was preferred over a higher order discretization scheme, to avoid convergence issues as such scheme is known to make calculations very stable. However, even if a 1st order discretization scheme can also produce diffusive results, as reported in (ANSYS Fluent 2016; Michalcová and Kotrasová 2020), the numerical results obtained in this work compared fairly well with experimental data, as demonstrated later in Section 5.

As mentioned previously, the RNG $k-\varepsilon$ turbulence model was considered here, with the enhanced wall treatment option. The output temperature, which affects the Nusselt number Nu, was closely monitored along with the residuals to make sure converged results were obtained. Re, heat transfer coefficient (h) and Nu are calculated as:

$$Re = \frac{UD_h}{v} \tag{4}$$

$$h = \frac{q}{\left(T_{plate} - T_m\right)} = \frac{q}{\left(T_{plate} - \frac{T_i + T_o}{2}\right)} \tag{5}$$

$$Nu = \frac{hD_h}{\lambda_{air}} \tag{6}$$

where U, D_h, v, q, T_{plate}, T_i, T_o, T_m and λ_{air} represent the bulk air velocity, channel hydraulic diameter, air kinematic viscosity, wall heat flux, absorber plate temperature, air temperature at

channel inlet, air temperature at channel outlet, mean air temperature and thermal conductivity of air, respectively.

4. MESH INDEPENDENCE STUDY

It is essential to generate a mesh offering accurate and mesh independent results. Insufficient (or sometimes too many) mesh refinements can produce erroneous results. Thus, a systematic mesh independence study has been carried out in this work. Meshes were refined several times until convergence of the results. Table 3 summarises the results of temperature, averaged heat transfer coefficient and averaged Nu at the absorber plate, obtained for three different mesh sizes. These simulations were run for $Re = 14{,}000$. The comparison of the predicted results shows that the results do not change significantly from the medium to the fine mesh, with a maximum change of about 1.5% in the results. Thus, the medium mesh is selected for rest of the simulations.

5. RESULTS AND DISCUSSION

Fluid flow and heat transfer predictions of the roughened solar air heater, selected for the current study, are discussed. The velocity contours along with streamlines, temperature and Nu contours and plots will be discussed separately.

5.1 CFD Model Validation

CFD-based numerical results are compared with the experimental data of Patel and Lanjewar (2019) in Figure 3. The averaged Nu is plotted against Re for different values of rib pitch to rib height ratio P/e. The corresponding averaged Nu values for the smooth absorber plate case are also included in Figure 3. The effect of ribs spacing is studied through considering P/e values of 6, 8, 10, 12 and 14, for Re ranging from 4,000 to 14,000. The comparison of the

thermal performance of SAH with and without roughness shows a significant enhancement in Nu values when V-shaped ribs are used on the absorber plate. The effect of the V-shaped roughness is however not too significant at low Re values. At Re = 4,000, the Nu values are slightly increased when V-shaped Ribs are present. An enhancement is observed for all P/e values, but the maximum enhancement is obtained for P/e = 10. Table 4 shows the percentage enhancement in Nu for all values of P/e. About 72.62% enhancement is obtained for Re = 12,000 and P/e = 10. Moreover, for P/e = 6 to 10, the first averaged Nu values increase to reach maximum values and then decrease for P/e = 10 to 14. Table 4 also tabulates the deviation of the predicted results from the experimental data. As can be seen, the numerical results match well the experimental data, with a percentage error under 8%. Figure 3 also shows that, in general, the averaged Nu increases with increasing Re. This confirms that a CFD-based approach can predict results close to the experimental work for this type of application.

5.2 Velocity Contours and Streamlines

Figure 4 shows a comparison of the velocity field on the central plane at the highest Re of each case, i.e. for Re = 14,000. The comparison is performed at P/e values of 6, 8, 10, 12 and 14. The rib pitch to rib height ratio P/e is an important parameter for a V-shaped roughened SAH as the formation of secondary flow regions and reattachment points depend on the ribs spacing. Low values of P/e ratio necessitate more ribs on the fixed length absorber plate with shorter distances between the ribs. The red color velocity contours show the free stream region, which is unaffected by the ribs. The main difference in the velocity contours visually comes in the ribs section, where the effect with increasing the P/e ratio is also evident.

Note that the laminar sublayer region of the boundary layer is disturbed by the presence of the ribs. Secondary flows and reattachment regions perturb the (thin) boundary layer, this results in the enhancement of the thermal performance. At low values of P/e ratio, the secondary flow

formed due to the first layer of ribs, quickly flows over the next rows of ribs as they are placed very close to each other. At moderate and high values of P/e, the secondary flow penetrates into the gap between the ribs and leads to the formation of reattachment points. The velocity gradients also decrease with an increase of P/e values. Figure 5 shows a comparison of the velocity field along with the streamlines on the central plane at Re = 14,000 and P/e values of 6, 8, 10, 12 and 14. The length of the recirculation regions increase with increasing values of P/e. It can also be seen that the reattachment points are not formed at P/e = 6. On the contrary, the working fluid needs to travel a longer distance after the reattachment points before striking the next row of ribs for P/e = 12 and 14. Both aforementioned situations lead to relatively lower overall heat transfer augmentations.

5.3 Temperature Contours

Figure 6 shows a comparison of the temperature on the absorber plate at Re = 14,000 for P/e values of 6, 8, 10, 12 and 14. The difference between the absorber plate temperature T_{plate} and mean air temperature T_m first decreases when P/e is changed from 6 to 10 and then increases when P/e is changed from 10 to 14. This shows an increase of Nu values with an increase of P/e values, with the maximum Nu values obtained at P/e = 10, where the temperature difference $T_{plate} - T_m$ is the lowest.

The cooling of the absorber plate is also affected by the change of the rib pitch to rib height ratio. The optimum plate cooling is achieved at P/e = 10. This can be linked to the interaction of the secondary flow with the main flow and the formation of reattachment points. At P/e = 10, the geometrical configurations seem adequate to ensure an efficient interaction of secondary and main flows before and after the reattachment points. This leads to a positive impact on the overall flow turbulence, decreasing the absorber plate temperature and increasing the Nu values.

It was shown in Figure 5 that the reattachment points were not formed at $P/e = 6$ and the working fluid needed to travel a longer distance after the reattachment points before striking the next row of ribs at $P/e = 12$ and 14. This leads here to relatively higher overall absorber plate temperature.

5.4 Local Nusselt Number Contours

Figure 7 shows a comparison of the local Nu contours on the absorber plate in the same conditions as before (Re = 14,000 for P/e values of 6, 8, 10, 12 and 14). The local Nu contours on the absorber plate show a strong dependency on P/e. The formation and interaction of the secondary flow regions and reattachment points depend on the ribs spacing, and thus affect the resulting Nu values. Nu is seen to increase because of the disturbance of the laminar sublayer regions. This increment in Nu as compared to the smooth absorber plate was shown in Figure 3. The Nu values first decrease when P/e is changed from 6 to 10 and then increase when P/e is changed from 10 to 14. The maximum Nu values are obtained at P/e = 10.

The reasons for the increasing and decreasing trend of Nu with increasing values of P/e were discussed previously in Section 5.2 (secondary flow effects). The dominant interaction of the secondary and main flows and the higher number of reattachment points at P/e = 10 lead to an optimum thermal performance.

Figure 8 shows a comparison of the numerically predicted averaged Nu values for different values of rib pitch to rib height ratio P/e. The averaged Nu values are plotted against Re values. It can be seen that Nu increases with increasing Re. This is due to the increase of turbulence with increasing Re. The maximum values of Nusselt number are observed at P/e = 10 and Re = 14,000.

CONCLUSIONS

Fluid flow and heat transfer characteristics of a roughened solar air heater with novel V-shaped ribs having staggered elements were investigated numerically. The thermal performance was established with and without roughness on the absorber plate. The ribs configurations were modified through changing the P/e ratio from 6 to 14. For each value of P/e ratio, numerical simulations were performed at Re = 4,000; 6,000; 8,000; 10,000; 12,000 and 14,000. The numerical results were then validated with the experimental data of Patel and Lanjewar (2019). From this work, the following conclusions can be drawn:

- The numerical results match well the experimental data, showing that CFD can be used to aid the design and development of SAHs, with optimized thermal efficiency. This also confirms the suitability of the RNG $k-\varepsilon$ turbulence model for this type of application.
- The rib pitch to rib height ratio P/e is found to be an important parameter in case of V-shaped roughened SAHs, as the formation of secondary flow regions and reattachment points depend on the ribs spacing.
- The lowest absorber plate temperature and maximum Nu values are found at rib pitch to height ratio of 10 and at Re = 12,000.
- About 72.6% enhancement of the thermal performance is obtained by applying a V-shaped roughness on the absorber plate at P/e = 10 and Re = 12,000.
- An increase of Re increases the fluid velocity, which decreases the absorber plate temperature, which in turn increases Nu.

REFERENCES

Alam, T., and Kim, M.H. 2017. A critical review on artificial roughness provided in rectangular solar air heater duct. Renew. Sust. Energ. Rev., 69:387-400. doi: 10.1016/j.rser.2016.11.192.

Alam, T., Saini, R.P., and Saini, J.S. 2014. Experimental investigation on heat transfer enhancement due to V-shaped perforated blocks in a rectangular duct of solar air heater. Energ. Convers. Manage., 81:374–383. doi: 10.1016/j.enconman.2014.02.044.

ANSYS Fluent, 2016. ANSYS Fluent User's Guide, ANSYS, Inc., Release 17.2.

Arunkumar, H.S., Karanth, K.V., and Kumar, S. 2020. Review on the design modifications of a solar air heater for improvement in the thermal performance. Sust. Energ. Technol. Assess., 39:100685. doi: 10.1016/j.seta.2020.100685.

Bisht, V.S., Patil, A.K., and Gupta, A. 2018. Review and performance evaluation of roughened solar air heaters. Renew. Sust. Energ. Rev., 81(1):954-977. doi: 10.1016/j.rser.2017.08.036.

Boonloi, A., and Jedsadaratanachai, W. 2016. Numerical investigation on turbulent forced convection and heat transfer characteristic in a square channel with discrete combined V-baffle and V-orifice. Case Stud. Therm. Eng., 8:226–235. doi: 10.1016/j.csite.2016.07.003.

Chamoli, S., and Thakur, N.S. 2013. Performance evaluation of solar air heater having V-down perforated baffles on the absorber plate. J. Renew. Sust. Energ., 5:063107. doi: doi.org/10.1063/1.4831780.

Chhaparwal, G.K., Srivastava, A., and Dayal, R. 2019. Artificial repeated-rib roughness in a solar air heater – A review. Sol. Energ., 194:329-359. doi: 10.1016/j.solener.2019.10.011

Close, D.J. 1963. Solar air heaters for low and moderate temperature applications. Sol. Energ., 7(3):117-124. doi: 10.1016/0038-092X(63)90037-9

Gawande, V.B., Dhoble, A.S., Zodpe, D.B., and Chamoli, S. 2016. A review of CFD methodology used in literature for predicting thermo-hydraulic performance of a roughened solar air heater. Renew. Sust. Energ. Rev., 54:550–605. doi: 10.1016/j.rser.2015.10.025

Jain, S.K., Agrawal, G.D., and Misra, R. 2019. A detailed review on various V-shaped ribs roughened solar air heater. Heat Mass Transf., 55:3369–3412. doi: 10.1007/s00231-019-02656-4.

Jin, D., Zhang, M., Wang, P., and Xu, S. 2015. Numerical investigation of heat transfer and fluid flow in a solar air heater duct with multi V-shaped ribs on the absorber plate. Energ., 89:1-13. doi: 10.1016/j.energy.2015.07.069.

Karmare, S.V., and Tikekar, A.N. 2010. Analysis of fluid flow and heat transfer in a rib grit roughened surface solar air heater using CFD. Sol. Energ., 84(40):9–17. doi: 10.1016/j.solener.2009.12.011.

Karwa, R., and Srivastava, V. 2013. Thermal performance of solar air heater having absorber plate with V-down discrete rib roughness for space-heating applications. J. Renew. Energ., 1-13:151578. doi: 10.1155/2013/151578.

Khanoknaiyakarn, C., Kwankaomeng, S., and Promvonge, P. 2011. Thermal performance enhancement in solar air heater channel with periodically V-shaped baffles. Proc. Int. Conf. Util Exhib Power Energy Syst Issues Prospect Asia, ICUE 2011, 3298352:1–6. doi: 10.1109/ICUEPES.2011.6497777.

Kumar, A., Avinash, S.K.B., and Badholiya, S.K. 2020. A critical review on performance of solar air heaters technologies and techniques. Int. J. Adv. Res. Ideas Innovations Technol., 6(2):334-354.

Kumar, A., Kumar, R., and Chauhan, R. 2017. Single-phase thermal and hydraulic performance analysis of a V-pattern dimpled obstacles air passage. Exp. Heat Transf., 30:393–426. doi: 10.1080/08916152.2016.1269139.

Kumar, A., Kumar, R., and Maithani, R. 2017. Correlation development for Nusselt number and friction factor of a multiple type V-pattern dimpled obstacles solar air passage. Renew. Energ., 109:461–479. doi: 10.1016/j.renene.2017.03.030.

Kumar, A., and Kim, M.H., 2015. Effect of roughness width ratios in discrete multi V-rib with staggered rib roughness on overall thermal performance of solar air channel. Sol. Energ., 119:399–414. doi: 10.1016/j.solener.2015.06.030.

Kumar, A., Saini, R.P., and Saini, J.S. 2014. Effect of roughness width ratio in discrete Multi v-shaped rib roughness on thermo-hydraulic performance of solar air heater. Heat Mass Transf., 51:209–220. doi: 10.1007/s00231-014-1407-0.

Kumar, R., Kumar, A., and Sharma, A. 2017. Experimental study of heat transfer enhancement in a rectangular duct distributed by multi V-perforated baffle of different relative baffle width. Heat Mass Transf., 53:1289–1304. doi: 10.1007/s00231-016-1901-7.

Kumar, S., and Saini, R.P. 2009. CFD based performance analysis of a solar air heater duct provided with artificial roughness. Renew. Energ., 34:1285–1291. doi: 10.1016/j.renene.2008.09.015.

Lau, S.C., Kukreja, R.T., and Mcmillin, R.D. 1991. Effects of V-shaped rib arrays on turbulent heat transfer and friction of fully developed flow in a square channel. Int. J. Heat Mass Transf., 34:1605–1616. doi: 10.1016/0017-9310(91)90140-A.

Maithani, R., and Saini, J.S. 2016. Heat transfer and friction factor correlations for a solar heater duct roughened artificially with V-ribs with symmetrical gaps. Exp. Therm. Fluid Sci., 70:220-227. doi: 10.1016/j.expthermflusci.2015.09.010.

Michalcová, V., and Kotrasová, K., 2020. The Numerical Diffusion Effect on the CFD Simulation Accuracy of Velocity and Temperature Field for the Application of Sustainable Architecture Methodology. Sust., 12:10173. doi: 10.3390/su122310173.

Promvonge, P. 2010. Heat transfer and pressure drop in a channel with multiple 60° V-baffles. Int. Comm. Heat Mass Transf., 37:835–840. doi: 10.1016/j.icheatmasstransfer.2010.04.003.

Patel, S.S., and Lanjewar, A. 2019. Experimental and numerical investigation of solar air heater with novel V rib geometry. J. Energ. Stor., 21:750-764. doi: 10.1016/j.est.2019.01.016.

Patel, S.S., and Lanjewar, A. 2018. Experimental analysis for augmentation of heat transfer in multiple discrete V-patterns combined with staggered ribs solar air heater. Renew. Energ. Focus, 25:31-39. doi: 10.1016/j.ref.2018.03.003.

Patil, A.K., Saini, J.S., and Kumar, K. 2012. Nusselt number and friction factor correlations for solar air heater duct with broken V-down ribs combined with staggered rib roughness. Renew. Sust. Energ. Rev., 4:033122. doi: 10.1063/1.4732133.

Ravi, R.K., and Saini, R.P. 2016. A review on different techniques used for performance enhancement of double pass solar air heaters. Renew. Sust. Energ. Rev., 56:941-952. doi: 10.1016/j.rser.2015.12.004.

Saxena, A., Varun, and El-Sebaii, A.A. 2015. A thermodynamic review of solar air heaters. Renew. Sust. Energ. Rev., 43:863-890. doi: 10.1016/j.rser.2014.11.059.

Selcuk, M.K. 1977. Solar air heaters and their applications. A.A.M. Sayigh (Ed.), Solar Energy Engineering, Academic Press, New York, Chapter 8.

Singh, I., and Singh, S. 2018. A review of artificial roughness geometries employed in solar air heaters. Renew. Sust. Energ. Rev., 92:405-425. doi: 10.1016/j.rser.2018.04.108.

Tanda, G. 2004. Heat transfer in rectangular channels with transverse and V-shaped broken ribs. Int. J. Heat Mass Transf., 47:229– 243. doi: 10.1016/S0017-9310(03)00414-9.

Yadav, A.S., Paul, A., and Sharma, P. 2013. CFD investigation of flow through an artificially roughened solar air heater. J. Sci. Technol., 2(3):16–9.

Yadav, A.S., and Thapak, M.K. 2014. Artificially roughened solar air heater: Experimental investigations. Renew. Sust. Energ. Rev., 36:370-411. doi: 10.1016/j.rser.2014.04.077.

Yadav, A.S., and Bhagoria, J.L. 2013. Heat transfer and fluid flow analysis of solar air heater: A review of CFD approach. Renew. Sust. Energ. Rev., 23:60–79. doi: 10.1016/j.rser.2013.02.035.

Yadav, A.S., and Bhagoria, J.L. 2013. A CFD (computational fluid dynamics) based heat transfer and fluid flow analysis of a solar air heater provided with circular transverse wire rib roughness on the absorber plate. Energ., 55:1127–42. doi: 10.1016/j.energy.2013.03.066.

Yadav, A.S., and Bhagoria, J.L. 2013. A CFD based heat transfer and fluid flow analysis of a Conventional solar air heater. J. Eng. Sci. Manage. Educ., 6(2):138–147.

Figure Legends

Figure 1: (a) Computational domain with boundary conditions and (b) schematics illustration of the mesh

Figure 2: (a) Computational domain with boundary conditions and (b) schematics illustration of the mesh

Figure 3: Nusselt number comparison for smooth and roughened SAH with p/e = (a) 6, (b) 8, (c) 10 (d) 12 and (14)

Figure 4: Comparison of velocity contours at Re = 14,000 for different values of P/e

Figure 5: Comparison of velocity contours along with streamlines at Re = 14,000 for different values of P/e

Figure 6*:* Comparison of temperature contours at Re = 14,000 for different values of P/e

Figure 7*:* Comparison of Nusselt number contours at Re = 14,000 for different values of P/e

Figure 8: Comparison of averaged Nusselt numbers for different values of P/e

Table 1: Geometric parameters of the computational domain

Symbol	**Parameter [Unit]**	**Value**
W	Width of the duct [mm]	300 mm
H	Height of the duct [mm]	25 mm
D_h	Hydraulic diameter [mm]	46.1 mm
L	Length of the duct [mm]	2350 mm
α	Angle of attack (degrees)	60^o
P/e	Rib pitch to rib height ratio [-]	6 - 14
g/e	Gap width to rib height ratio [-]	4
e/D_h	Rib height to hydraulic diameter ratio [-]	0.043
P'/P	Position of staggered element to rib pitch ratio [-]	0.40
r/e	Size of staggered element to height of the rib ratio [-]	4
d/w	Position of gap to vertical length of symmetrical rib elements [-]	0.65
g′/e	Width of the relative gap in each symmetrical rib elements [-]	1
Re	Reynolds Number [-]	4000 - 14000

Table 2: Geometric parameters of different cases

Case	P/e	P (mm)	P' (mm)
I	6	11.91	4.76
II	8	15.88	6.35
III	10	19.85	7.94
IV	12	23.81	9.54
V	14	27.78	11.11

Table 3: Mesh Independence Test

Grid Size	No of Nodes	No of Elements	Temperature of absorber plate (K)	Heat Transfer coefficient (W/m^2K)	Nusselt Number
Coarse	1,958,085	5,363,120	330.51	41.051	78.2
Medium	2,432,671	6,696,404	330.20	41.58	79.2
Fine	3,178,245	8,764,343	330.14	41.68	79.4

Table 4: Comparison of experimental results of Patel and Lanjewar [7] with a smooth solar air heater at different Reynolds numbers

Re	Percentage deviation from the experimental data (%)					Increase in Nusselt number (%)				
	I	II	III	IV	V	I	II	III	IV	V
4000	7.00	5.68	7.00	2.04	3.96	7.30	3.83	1.97	11.24	4.54
6000	3.69	2.55	2.59	2.44	2.95	29.17	31.15	42.56	41.75	38.96
8000	2.60	2.35	6.96	4.41	4.28	42.09	49.16	53.74	49.65	46.92
10000	5.64	5.48	5.35	5.7	7.47	48.31	54.39	69.34	63.36	49.26
12000	6.00	6.50	6.34	6.37	7.61	53.42	55.8	72.62	61.83	50.21
14000	7.00	6.90	7.12	7.5	7.65	53.79	55.77	71.09	57.63	50.18

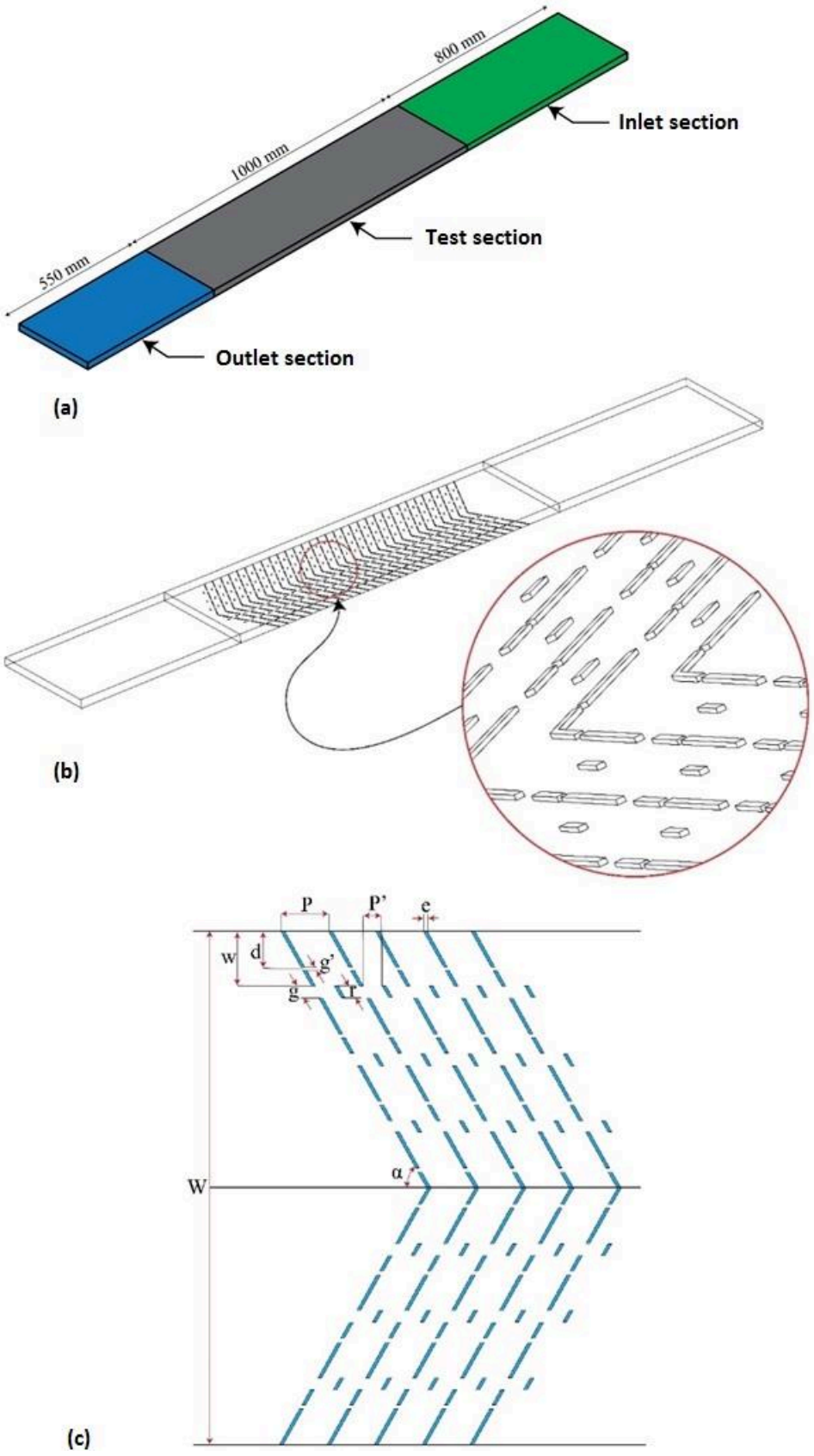

Figure 1: (a) Computational domain with boundary conditions and (b) schematics illustration of the mesh

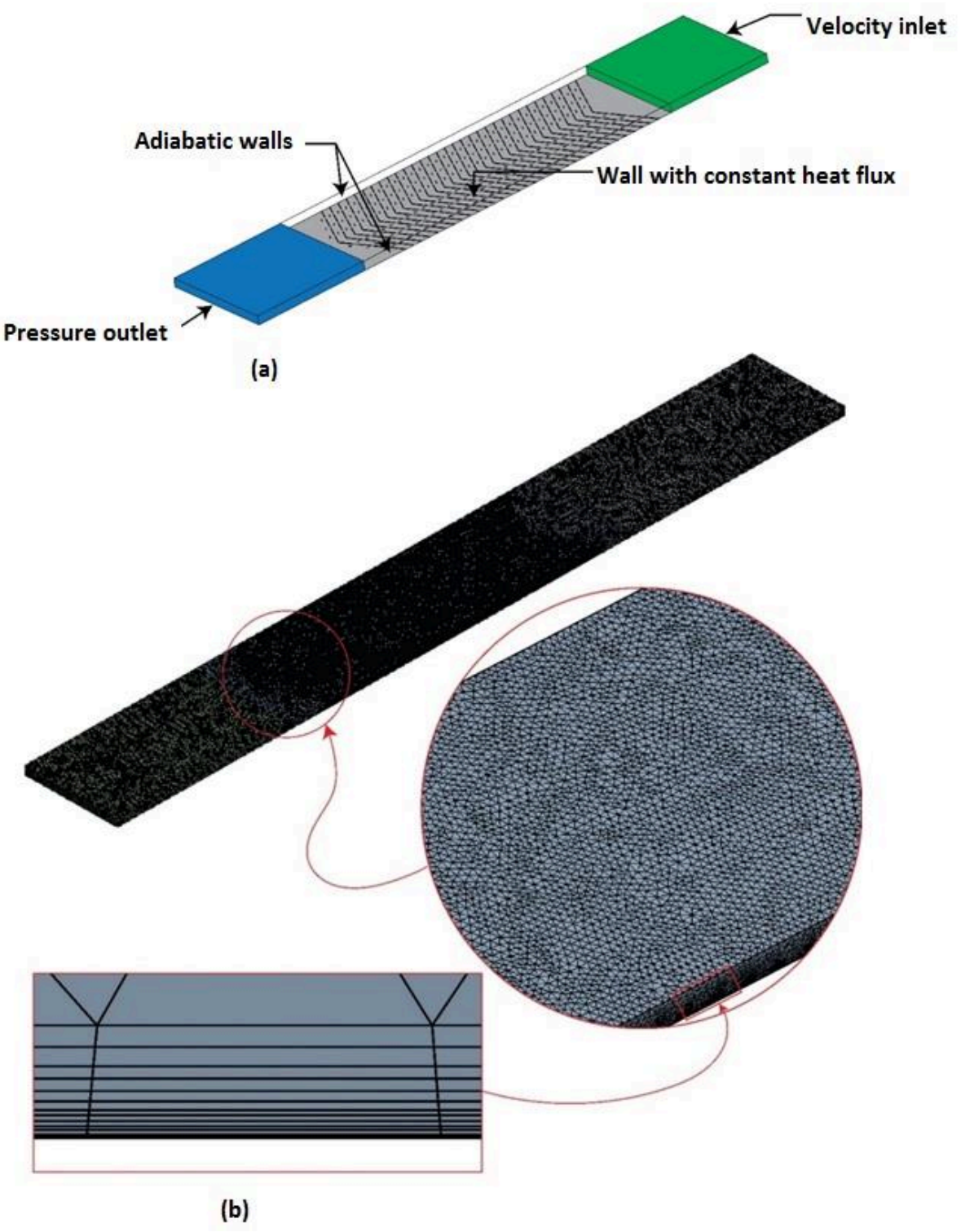

Figure 2: (a) Computational domain with boundary conditions and (b) schematics illustration of the mesh

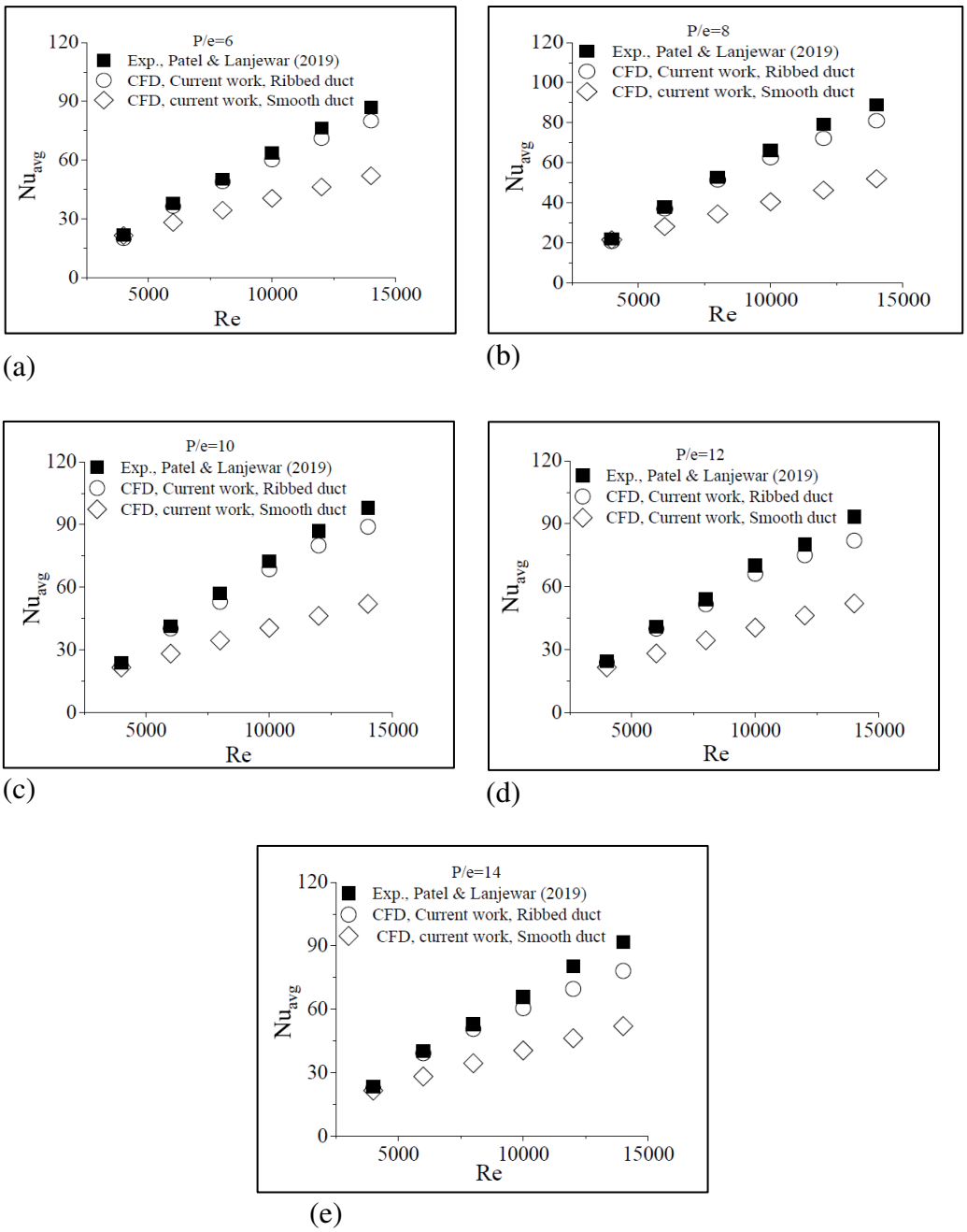

Figure 3: Nusselt number comparison for smooth and roughened SAH with p/e = (a) 6, (b) 8, (c) 10 (d) 12 and (14)

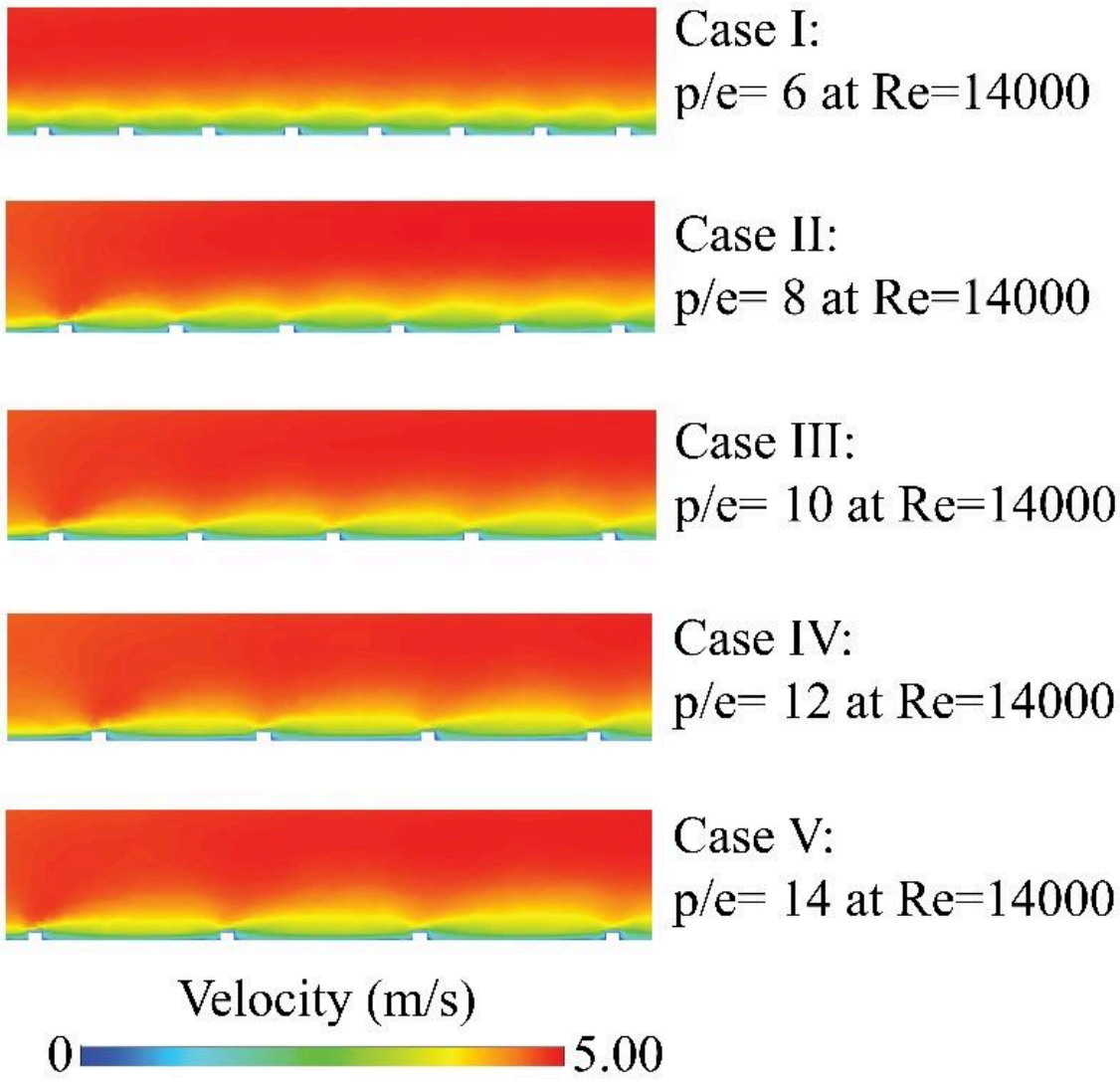

Figure 4: Comparison of velocity contours at Re = 14,000 for different values of P/e

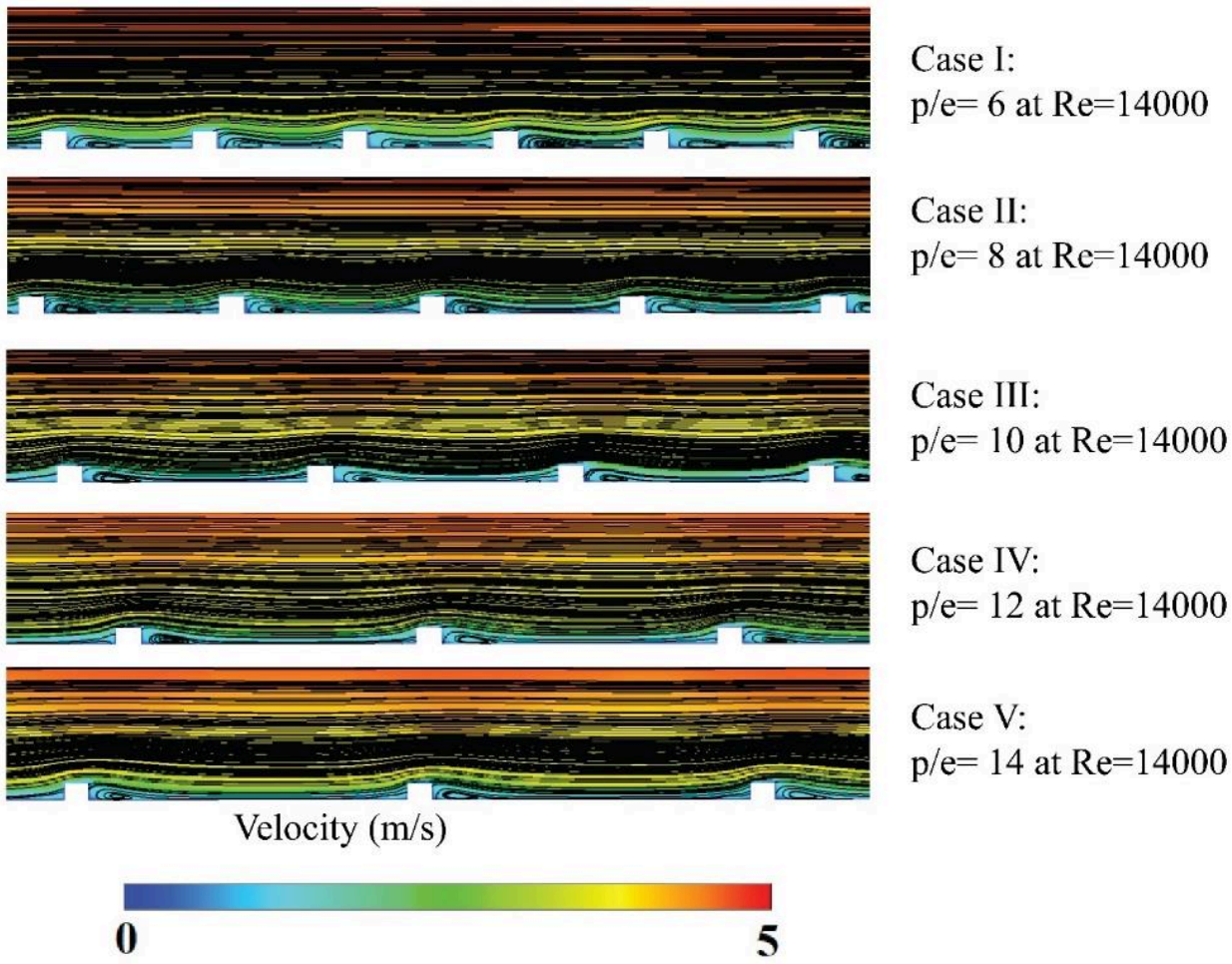

Figure 5: Comparison of velocity contours along with streamlines at Re = 14,000 for different values of P/e

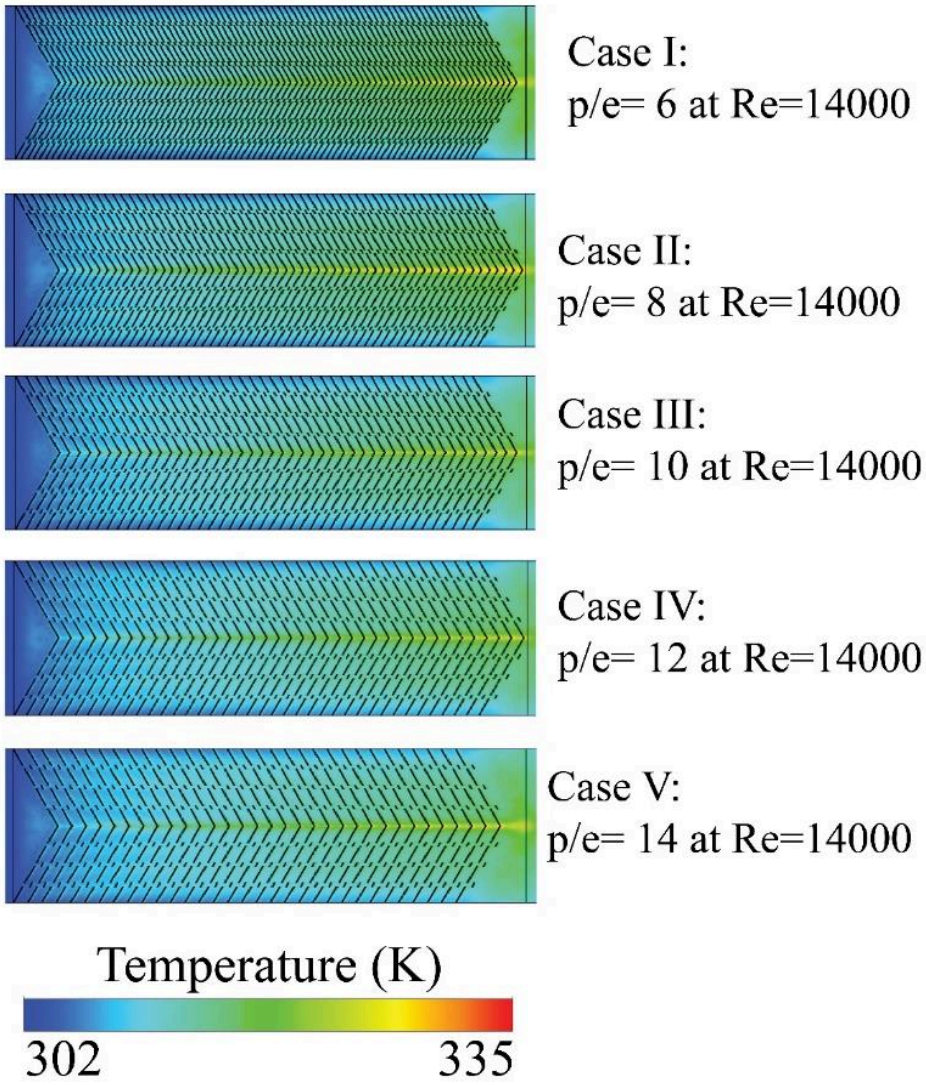

Figure 6*:* Comparison of temperature contours at Re = 14,000 for different values of P/e

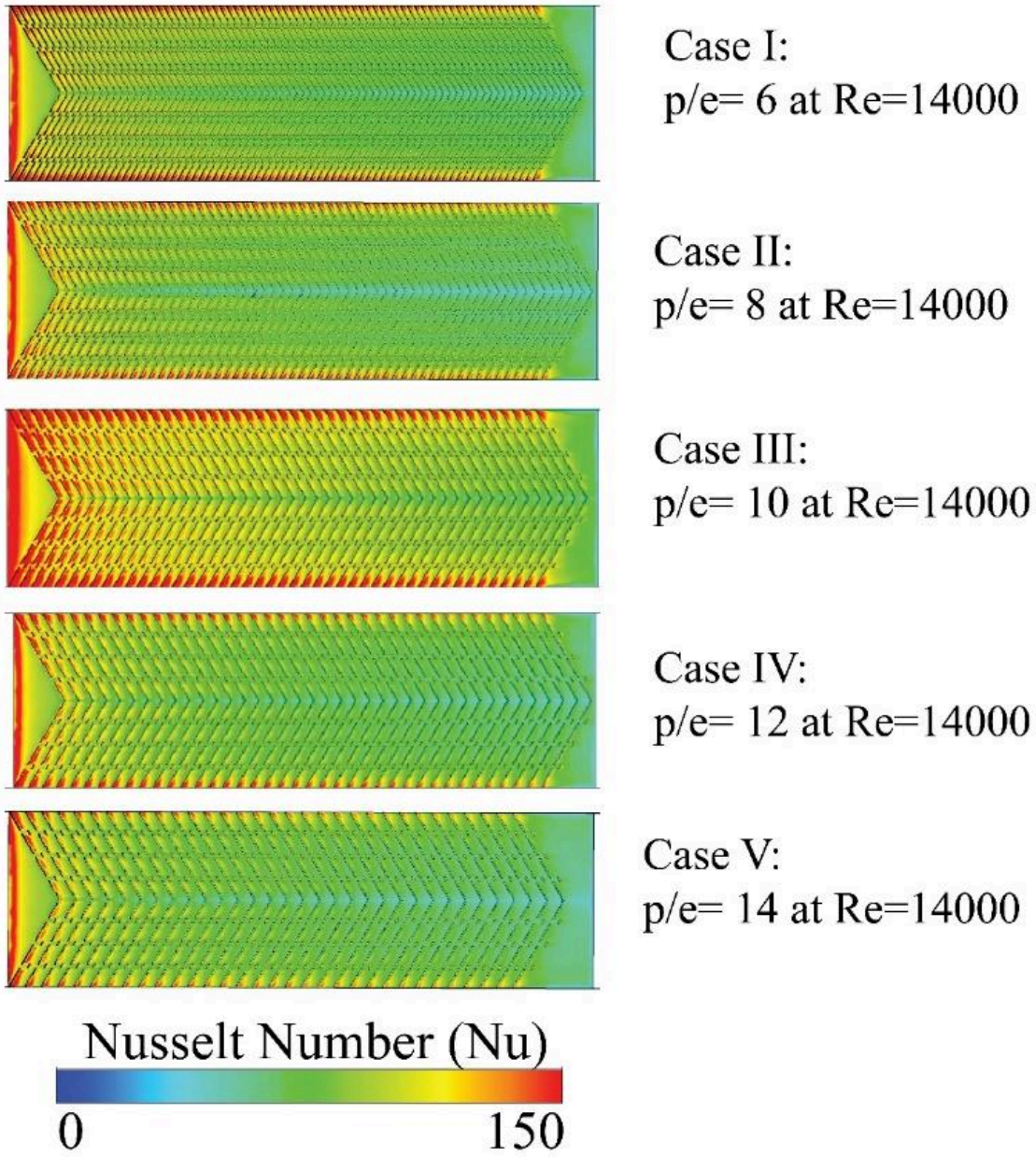

Figure 7*:* Comparison of Nusselt number contours at Re = 14,000 for different values of P/e

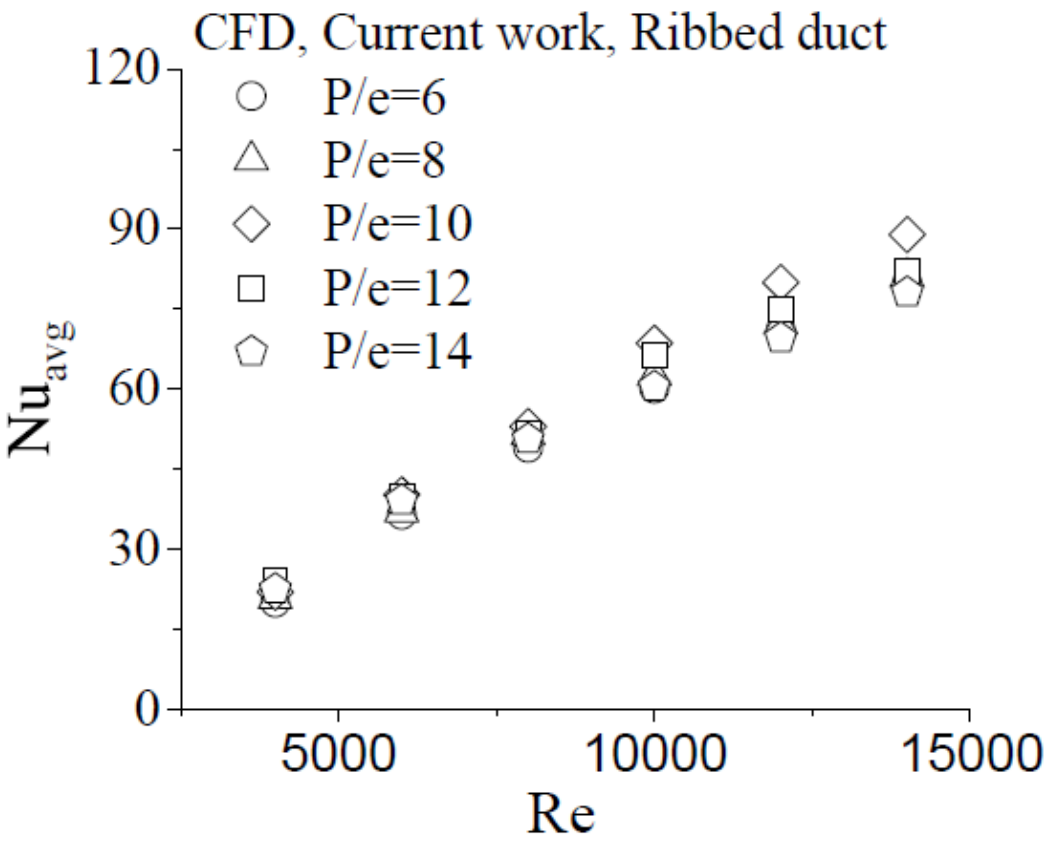

Figure 8: Comparison of averaged Nusselt numbers for different values of P/e